

The effects of internal refractive index variation in near-infrared optical tomography: a finite element modelling approach

Hamid Dehghani¹, Ben Brooksby¹, Karthik Vishwanath²,
Brian W Pogue¹ and Keith D Paulsen¹

¹ Thayer School of Engineering, Dartmouth College, Hanover, New Hampshire 03755, UK

² Department of Physics and Astronomy, Dartmouth College, Hanover, New Hampshire 03755, UK

Received 5 May 2003, in final form 20 June 2003

Published 30 July 2003

Online at stacks.iop.org/PMB/48/2713

Abstract

Near-infrared (NIR) tomography is a technique used to measure light propagation through tissue and generate images of internal optical property distributions from boundary measurements. Most popular applications have concentrated on female breast imaging, neonatal and adult head imaging, as well as muscle and small animal studies. In most instances a highly scattering medium with a homogeneous refractive index is assumed throughout the imaging domain. Using these assumptions, it is possible to simplify the model to the diffusion approximation. However, biological tissue contains regions of varying optical absorption and scatter, as well as varying refractive index. In this work, we introduce an internal boundary constraint in the finite element method approach to modelling light propagation through tissue that accounts for regions of different refractive indices. We have compared the results to data from a Monte Carlo simulation and show that for a simple two-layered slab model of varying refractive index, the phase of the measured reflectance data is significantly altered by the variation in internal refractive index, whereas the amplitude data are affected only slightly.

(Some figures in this article are in colour only in the electronic version)

1. Introduction

The use of light in both diagnosis and treatment has grown rapidly over the past few decades. One example incorporates the use of near-infrared (NIR) light as a physiological probe (NIR spectroscopy) and imaging tool (NIR tomography) for biological tissue, particularly with applications for the female breast (Dehghani *et al* 2003b, Fantini *et al* 1998, Hebden *et al* 2001, Chance 2001), neonatal head (Hebden *et al* 2003), adult head (Bluestone *et al* 2001),

human muscle (Hillman *et al* 2001), and small animal imaging for research of disease (Xu *et al* 2003). Typically, light is delivered to the tissue using a set of optical fibres, while exiting light, which has propagated through the tissue, is collected at a number of other locations using optical fibres or imaging optics. In the case of tomography, a set of measurements is made at the surface of the tissue for each applied source. These measurements, also known as the boundary data, are then used to estimate the internal optical properties of tissue, which would have caused the recorded changes in the remitted light. Once transmission measurements are acquired, it has been established that quantitatively accurate estimates of the absorption and reduced scattering coefficients in tissue can be determined through the appropriate model-based fitting of the data (Fantini *et al* 1998, Delpy and Cope 1997, McBride *et al* 1999, Godavarty *et al* 2002). If NIR measurements are obtained at a sufficient number of wavelengths, the calculated optical properties can be used to derive physiological properties of the tissue under investigation, namely, total haemoglobin, oxygen saturation, water and lipid concentrations (Mcbride *et al* 2002). This makes NIR tomography a promising imaging modality, since it can provide functional information about the region under investigation. One issue that has not received adequate attention in optical tomography is the inclusion of index of refraction variation as a parameter in accurate numerical modelling which influences image reconstruction. In this study, the effect of index of refraction changes in tissue simulating models is evaluated and a theoretical basis for numerical modelling the appropriate response is established.

In order to determine internal optical properties of tissue, and therefore, accurate functional information about the region of interest, an accurate model of light propagation is essential. The most widely used model of light propagation within tissue is the diffusion approximation to the radiative transport equation (RTE), which under certain conditions is an accurate simplification (Arridge 1999). In the cases where the diffusion model is expected to fail, for example when imaging the adult or neonatal head, either the full RTE is preferred (Klose and Hielscher 1999) or some hybrid diffusion/radiosity model has been recommended (Arridge *et al* 2000). It is generally agreed that stochastic models such as Monte Carlo methods provide the most accurate prediction of light transport, but suffer from long computation times and complex coding challenges when significant heterogeneity exists, making them predominantly useful for scientific validation studies. Generally, however, while tissue light propagation models allow inhomogeneity in optical absorption and scattering, the refractive index, n , is assumed to be constant throughout the domain at a value representative of biological tissue (typically $n = 1.33$). Although the actual absolute value of tissue refractive index is debatable (due to difficulties in obtaining accurate data), it is widely accepted that these values differ between tissues. In bulk tissues, the index of refraction is intimately tied to the overall reduced scattering coefficient, as the microscopic fluctuations in the index between membranes and structural components of tissue cause the scattering that is dominant in the light–tissue interaction. However, changes in n also exist at macroscopic scales, for example, at interfaces between larger tissue structures (types), which change the speed of light creating effects that are not modelled in many cases. Most work reported to date involving incoherent light, has been confined to computations which consider a single wave speed (constant refractive index). Although some progress has been described in deriving an approximation to the RTE which incorporates refractive index inhomogeneity (Khan and Jiang 2003), few results have been shown to date which identify the effect of internal refractive index variation on boundary measurements. Some work, however, has been done which looks at various implementations of internal boundary conditions within a diffusion model that accounts for internal refractive index variation (Aronson 1995, Faris 2002), as well as analytical solutions which aim to recover optical properties of a single circular infinite central anomaly (Walker *et al* 1998). Further work

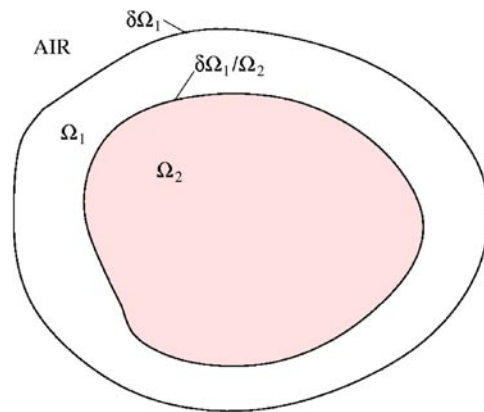


Figure 1. A domain Ω containing regions of different refractive indices, Ω_1 and Ω_2 .

has also been performed in incorporating boundary conditions into scattering surface integral equations for diffuse waves in the case of index mismatch media (Ripoll and Nieto-Vesperinas 1999).

In this work, a diffusion equation finite element model is developed where the effects of piecewise constant internal refractive index variations are treated through incorporation of appropriate internal boundary conditions which generate a discontinuity in the photon density field at the interface between step changes in refractive index. The numerical implementation is described, and comparison with Monte Carlo model predictions is presented. The data indicate that for frequency-domain measurements, both the amplitude and phase of measured data are altered by internal variation in refractive index with the phase measurements showing the largest effect.

2. Theory

2.1. Diffusion approximation

It is generally accepted that if the magnitude of the isotropic fluence within tissue is significantly larger than the directional flux magnitude, the light field is 'diffuse', which occurs when the scattering interaction dominates over absorption in a region of interest. Mathematically, this assumption allows a transition from the Boltzmann transport equation, which is used to describe an anisotropic light field to the diffusion equation approximation. The diffusion approximation in the frequency domain is given by

$$-\nabla \cdot \kappa(r) \nabla \Phi(r, \omega) + \left(\mu_a(r) + \frac{i\omega}{c_m(r)} \right) \Phi(r, \omega) = q_0(r, \omega) \quad (1)$$

where μ_a and μ'_s are absorption and reduced scattering respectively, $q_0(r, \omega)$ is an isotropic source, $\Phi(r, \omega)$ is the photon fluence rate at position \mathbf{r} , $\kappa = \frac{1}{3(\mu_a + \mu'_s)}$ is the diffusion coefficient and $c_m(r)$ is the speed of light in the medium at any point, defined by $c/n(r)$, where $n(r)$ is the index of refraction at the same point and c is the speed of light in vacuum.

The best description of the air-tissue boundary, $\partial\Omega_1$ in figure 1, is derived with an index-mismatched type III condition, in which the fluence at the edge of the tissue exits and does not return (Schweiger *et al* 1995). The flux leaving the external boundary is equal to the fluence

rate at the boundary weighted by a factor that accounts for the internal reflection of light back into the tissue. This relationship is described in the following equation:

$$\Phi(\xi, \omega) + 2A\hat{\mathbf{n}} \cdot \kappa(\xi)\nabla\Phi(\xi, \omega) = 0 \quad (2)$$

where ξ is a point on the boundary ($\partial\Omega_1$), and A depends upon the relative refractive index (RI) mismatch between tissue Ω_1 and air. A can be derived from Fresnel's law:

$$A = \frac{2/(1 - R_0) - 1 + |\cos\theta_c|^3}{1 - |\cos\theta_c|^2} \quad (3)$$

where $\theta_c = \arcsin(n_{\text{AIR}}/n_1)$, the angle at which total internal reflection occurs for photons moving from region Ω_1 with RI n_1 to air with RI n_{AIR} , and $R_0 = \frac{(n_1/n_{\text{AIR}} - 1)^2}{(n_1/n_{\text{AIR}} + 1)^2}$. At the external boundaries, $n_{\text{AIR}} = 1$, the RI of free space.

At interior nodes, which lie on an interface between two media with different indices of refraction, $\partial\Omega_1/\Omega_2$ in figure 1, we apply the conditions used by Schmitt *et al* (1990) and Takatani and Graham (1979) and Faris (2002):

$$\hat{\mathbf{n}} \cdot D_1\nabla\Phi_1(\xi, \omega) = \hat{\mathbf{n}} \cdot D_2\nabla\Phi_2(\xi, \omega) \quad (4)$$

$$\frac{\Phi_1(\xi, \omega)}{\Phi_2(\xi, \omega)} = \left(\frac{n_1}{n_2}\right)^2. \quad (5)$$

These equations enforce continuity in the flux across a step change in n , and establish a corresponding discontinuity in the fluence based upon the two refractive indices defining the regions separating the boundary.

2.2. Finite element implementation

When the refractive index is homogeneous, the finite element discretization of Ω (where $\Omega = \Omega_1 \cup \Omega_2$) can be obtained by subdividing the domain into D elements joined at V vertex nodes. In finite element formalism, $\Phi(\mathbf{r})$ is approximated by the piecewise continuous polynomial function $\Phi^h(\mathbf{r}, \omega) = \sum_i^V \Phi_i u_i(\mathbf{r})\Omega^h$, where Ω^h is a finite-dimensional subspace spanned by basis functions $\{u_i(\mathbf{r}); i = 1, \dots, V\}$ chosen to have limited support. The problem of solving for Φ^h becomes one of sparse matrix inversion: in this work, we use biconjugate gradients stabilized solver. As developed previously (Paulsen and Jiang 1995, Arridge *et al* 1993), the diffusion equation in the FEM framework can be expressed as a system of linear algebraic equations:

$$\left(K(\kappa) + C\left(\mu_a + \frac{i\omega}{c_m}\right) + \frac{1}{2A}F\right)\Phi = q_0 \quad (6)$$

where the matrices $K(\kappa)$, $C\left(\mu_a + \frac{i\omega}{c_m}\right)$ and F have entries given by

$$K_{ij} = \int_{\Omega} \kappa(r)\nabla u_i(r)\nabla u_j(r) d^n r \quad (7)$$

$$C_{ij} = \int_{\Omega} \left(\mu_a(r) + \frac{i\omega}{c_m(r)}\right) u_i(r)u_j(r) d^n r \quad (8)$$

$$F_{ij} = \oint_{\partial\Omega} u_i(r)u_j(r) d^{n-1}r \quad (9)$$

and the source vector q_0 has terms

$$q_{0i} = \int_{\Omega} u_i(r)q_0(r) d^n r. \quad (10)$$

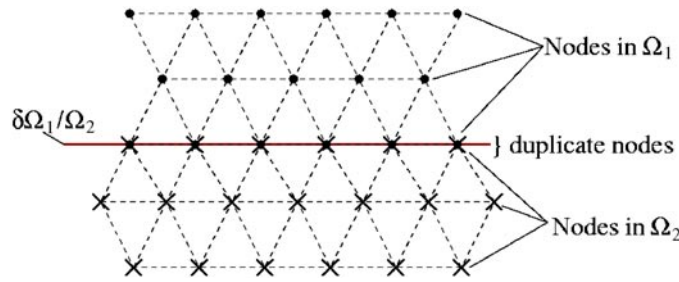


Figure 2. Meshing the interface between two regions of different refractive indices. Note that the nodes on the boundary $\delta\Omega_1/\Omega_2$ are duplicated to allow the enforcement of internal boundary conditions.

2.3. Diffusing medium with internal refractive index boundary

In the presence of piecewise linear change in internal refractive index, the continuity of Φ throughout the computational domain implied in equation (6) must be modified to allow two values to coexist at nodes in the mesh resident at a refractive index interface. This can be achieved conceptually (and practically) by generating coincident but duplicate nodes at the discretized points forming the boundary between two regions of distinct refractive index which represent the two degrees of freedom contained in the solution space defined by equations (4) and (5). Here, the duplicate nodes on the internal boundary are assigned to the elements that belong to either domain Ω_1 or Ω_2 which have the corresponding RI value associated with that region, figure 2. This allows two values of Φ to simultaneously coexist in the list of unknowns at the index-mismatched interface. On matrix assembly, coupling across the interface is accomplished through the use of a continuous weighting function pre-selected to correspond to one of the node numbers associated with the duplicate pair creating a row location in the discretized version of equation (6) on the interface. The row number associated with the partnered node is initially empty. Therefore, to complete the algebraic system, the explicit enforcement of equation (5) can be rewritten as

$$\Phi_1 - \left(\frac{n_1}{n_2}\right)^2 \Phi_2 = 0 \tag{11}$$

and enforces the required discontinuity in Φ .

Alternatively, the extra degree of freedom associated with the interface discontinuity in Φ can be eliminated during element-by-element assembly of C_{ij} in equation (8) through indirect enforcement of equation (11) based on logical decision making. For example, assume that the Φ -value of the higher region number in figure 2 is retained during matrix assembly, then if neither i or j in equation (8) is on the interface or i is on the interface but j is in the pre-selected (higher numbered) region (region 2 in figure 2), equation (8) applies. However, if i is on the interface but j is in the lower numbered region (region 1) then equation (8) becomes

$$C_{ij} = \int_{\Omega_1} \left(\mu_a(r) + \frac{i\omega}{c_m(r)}\right) u_i(r) \left(\frac{n_1}{n_2}\right)^2 u_j(r) d^n r \tag{12}$$

where Ω_1 implies integration over the region 1 elements containing node j . If both i and j reside on the interface then equation (8) is assembled as

$$C_{ij} = \int_{\Omega_1} \left(\mu_a(r) + \frac{i\omega}{c_m(r)}\right) u_i(r) \left(\frac{n_1}{n_2}\right)^2 u_j(r) d^n r + \int_{\Omega_2} \left(\mu_a(r) + \frac{i\omega}{c_m(r)}\right) u_i(r) u_j(r) d^n r. \tag{13}$$

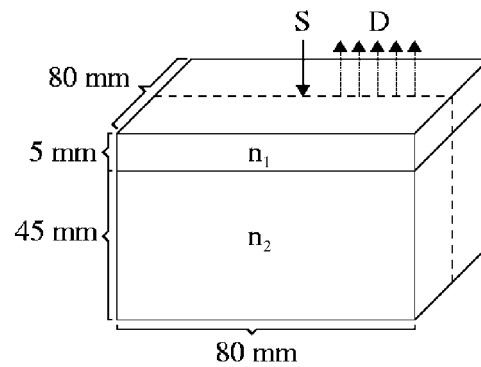


Figure 3. Geometry of the model used both for FEM and Monte Carlo simulations. The two-layered slab has a width and length of 80 mm and a thickness of 50 mm. The top layer has a thickness of 5 mm, with each layer having the same optical absorption and scatter, but allowed different refractive indices. The source is placed at the centre of the topmost face, and reflectance measurements are calculated at 1 mm intervals, spanning distances of 10–29 mm away from the source. The dashed line represents the slice at which the internal field distributions are shown in figures 6 and 7.

The solution that results produces interface values of Φ associated with the higher numbered region and the corresponding values for the partnered side can be retrieved from equation (11) once Φ_2 is known.

2.4. Monte Carlo modelling

A Monte Carlo model to simulate propagation of light in a semi-infinite turbid medium was extended to photon propagation in a stratified medium as described previously (Wang *et al* 1995, Vishwanath *et al* 2002). Briefly, the turbid medium was modelled as having layers of finite thickness (along the z -axis) with specified transport coefficients and refractive indices in each layer. Photons were incident normally at the top face of the turbid medium. For every scattering event where the calculated step size (s) (along a particular direction) caused a photon to cross an index-mismatched boundary, the photon was first propagated to the point where its trajectory intersected the boundary via a shortened step size (s_1). The angle of incidence with respect to $\pm z$ -axis (depending on the direction of photon travel) was computed and used to determine if the photon suffered total internal reflection (from Snell's law). If the photon was internally reflected, then the z -component of the photon's travel direction was reversed and the photon completed the remainder of the step ($s - s_1$) in the same layer, otherwise the reflection coefficient from Fresnel's equations was computed and compared against a uniformly generated random number. For every sampling of the random number that was less than the reflection coefficient, the photon underwent total internal reflection, otherwise it was transmitted to the next layer (or escaped from the domain). On transmission into a different layer the final spatial location of the photon was calculated by propagating the photon by a distance of $s - s_1$ that was adjusted in length (to account for the difference in transport coefficients between the two layers) and its direction corrected to consider refraction. All photons emanating from the top layer of the turbid medium were spatially and temporally binned to calculate the reflectance from a turbid medium. The resulting temporal data were Fourier transformed to give frequency-domain estimates of the amplitude and phase shift as a function of distance, in order to match the type of data used in our tomography system.

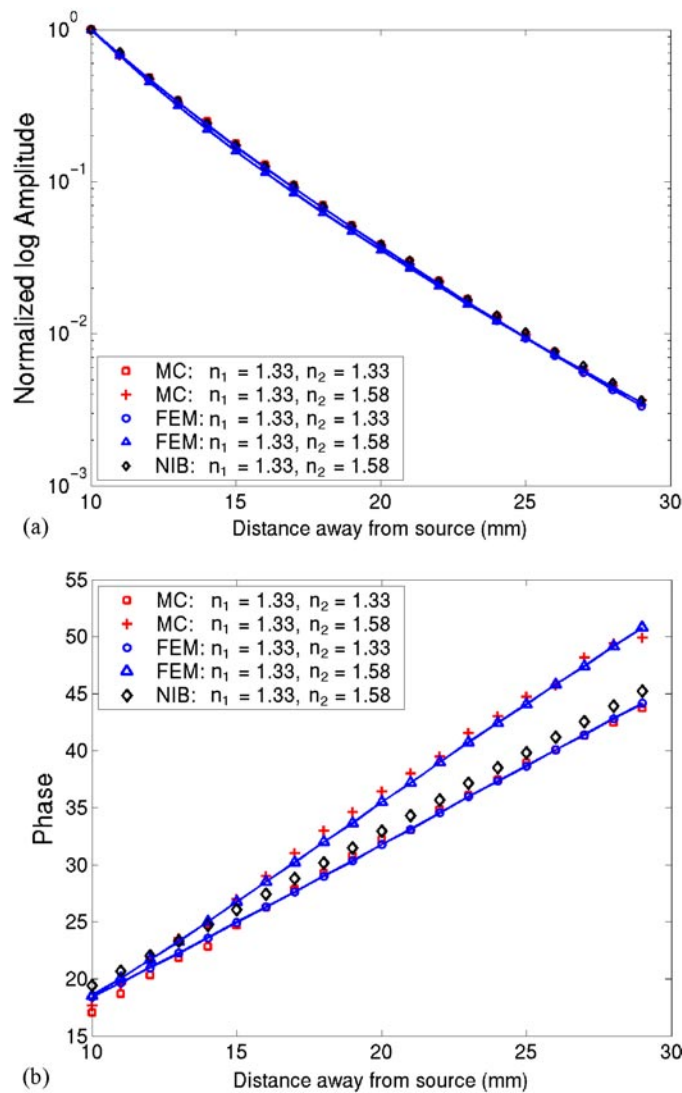


Figure 4. (a) Amplitude and (b) phase of the measured signal at detector positions for both the FEM and Monte Carlo models where $n_1 = n_2 = 1.33$, and $n_1 = 1.33$ and $n_2 = 1.58$. Calculated data from the FEM model, with no internal boundary conditions are also shown.

3. Results

In the following sections, we compare the results from the modified diffusion model, standard diffusion model and Monte Carlo model for a simple two-layered slab of either homogeneous or inhomogeneous internal RI values. All calculations were performed on a 1.7 GHz Xenon PC running Linux with 2 Gbytes of RAM.

The FEM simulations were completed with NIRFAST (Near InfraRed Frequency-domain Absorption and Scatter Tomography), which is a frequency-domain FEM code that can also be used for inverse problems in NIR optical tomography (Dehghani *et al* 2003b, 2003a). The code has been modified to incorporate internal boundaries and therefore duplicate nodes at an

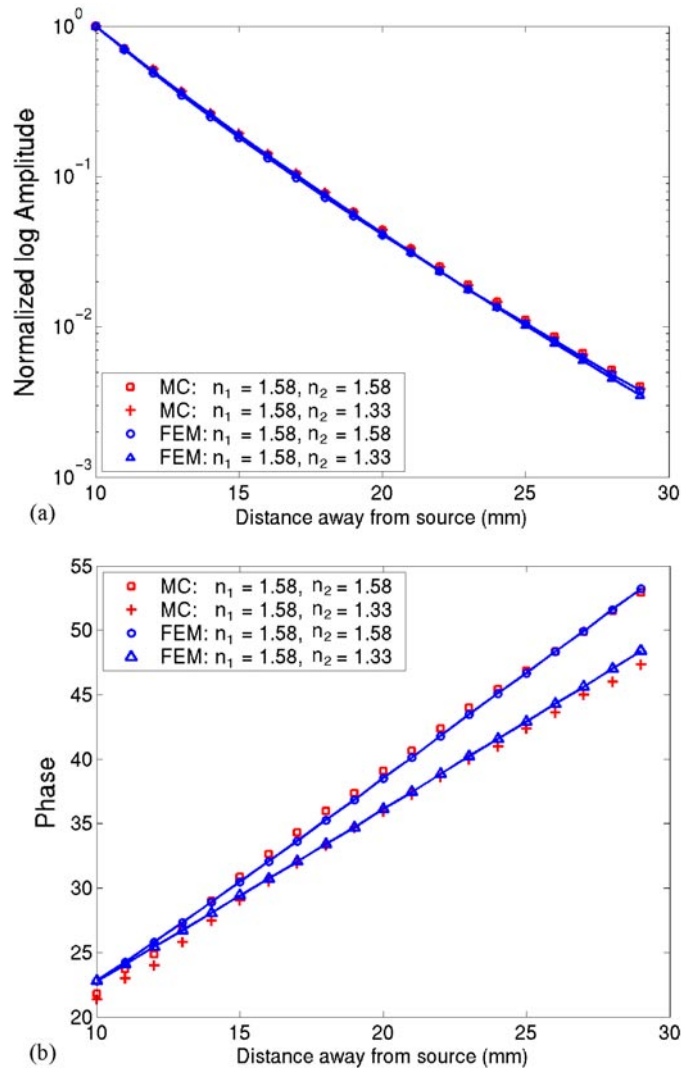


Figure 5. (a) Amplitude and (b) phase of the measured signal at detector positions for both the FEM and Monte Carlo models where $n_1 = n_2 = 1.58$, and $n_1 = 1.58$ and $n_2 = 1.33$.

internal interface representing an RI change. Three-dimensional meshes were created using NETGEN (Schoberl).

For the Monte Carlo results, the number of simulated photons was 50×10^6 . The total execution time was about two days, and the results produced time-resolved data at detector positions.

The model domain was a slab with a width and length of 80 mm and a thickness of 50 mm, figure 3. The source was placed at the centre of the topmost boundary and measurements were made at 1 mm distances from 10 to 29 mm away from the source. The model consisted of two layers, the top layer having a thickness of 5 mm, and the bottom layer a thickness of 45 mm. The optical properties were homogeneous, with $\mu_a = 0.01 \text{ mm}^{-1}$ and $\mu'_s = 1 \text{ mm}^{-1}$. The refractive index of each layer was varied to create matched or mismatched phantoms.

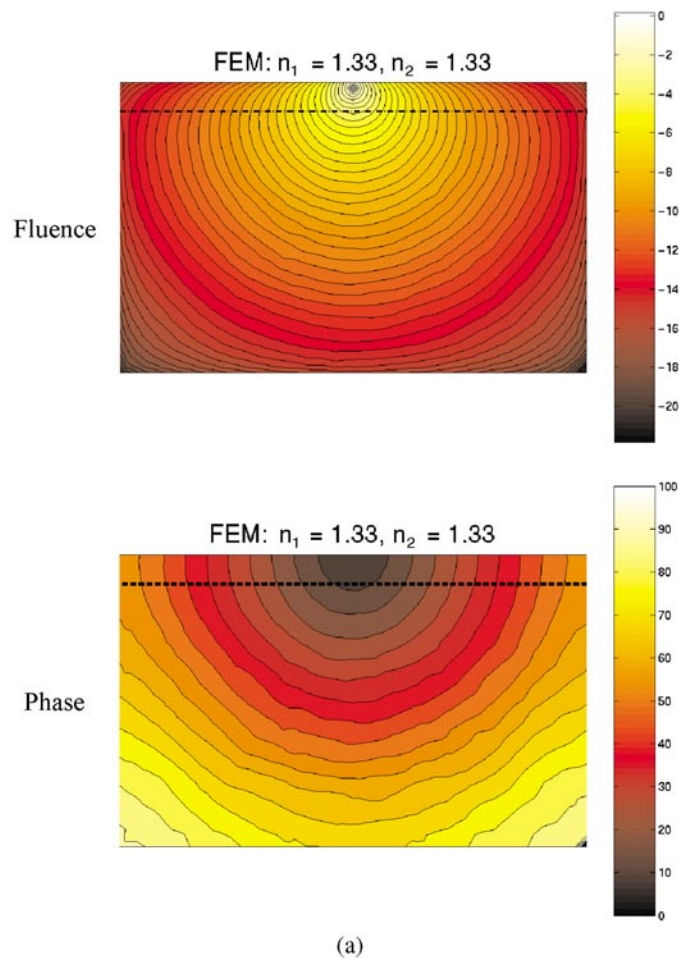


Figure 6. The internal fluence amplitude and phase distribution when (a) $n_1 = n_2 = 1.33$, and (b) $n_1 = 1.33$ and $n_2 = 1.58$. The plot represents the distribution in the cross-section shown by the dashed lines in figure 3. Also shown in (c) is the result from the FEM model with no internal boundary conditions.

In the first dataset, results were calculated for $n_1 = n_2 = 1.33$, as well as when $n_1 = 1.33$ and $n_2 = 1.58$. The FEM mesh used in the calculations which assumed no internal boundaries, i.e. no duplicate nodes, consisted of 16 848 nodes corresponding to 73 308 linear tetrahedral elements, while for the case where internal boundaries were modelled, the mesh consisted of 21 024 nodes corresponding to 73 308 linear tetrahedral elements. Data were calculated for a single source, as shown in figure 3, and reflectance measurements were obtained at discrete points on the same surface, 10 to 29 mm away from the source. The results are shown in figures 4(a) and (b) for amplitude and phase, respectively.

Results were also calculated when $n_1 = n_2 = 1.58$, as well as when $n_1 = 1.58$ and $n_2 = 1.33$. The FEM mesh used for these calculations was exactly the same as that noted above. The results are shown in figures 5(a) and (b) for amplitude and phase, respectively.

Figures 6 and 7 show the cross-section of internal intensity and phase plots directly under the source at $y = 0$ mm (shown as dashed lines in figure 3). In figure 6(a), the cross-section

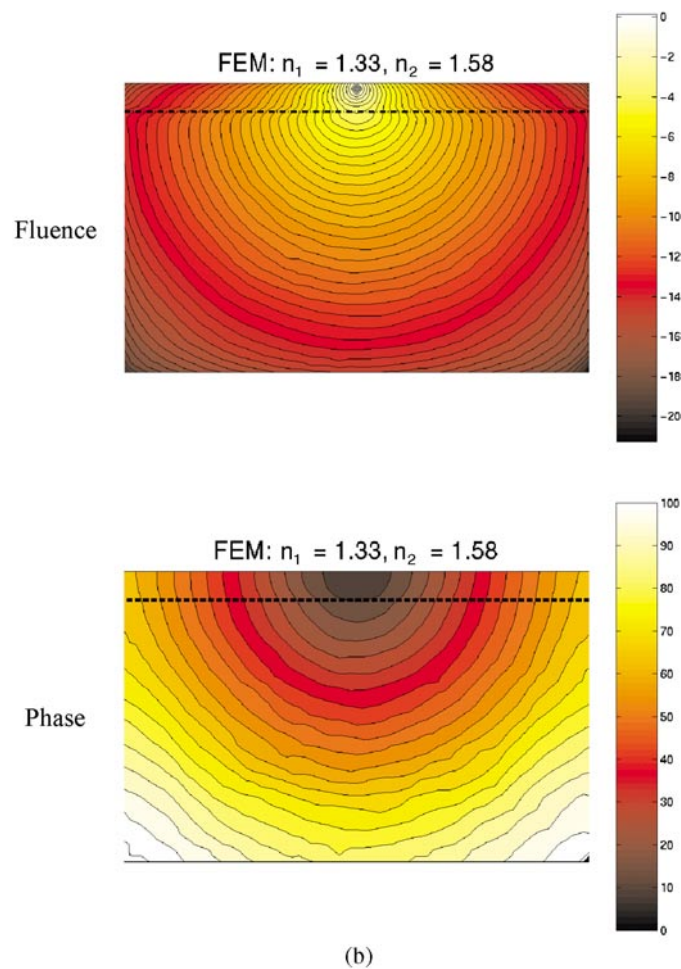


Figure 6. (Continued.)

of the fluence field and phase are shown when $n_1 = n_2 = 1.33$, where the magnitude is colour coded. In figure 6(b), the optical fluence and phase plot for $n_1 = 1.33$ and $n_2 = 1.58$ is presented. In figure 6(c), the corresponding optical fluence and phase plot for $n_1 = 1.33$ and $n_2 = 1.58$ is shown, but in this case, no internal boundary (NIB) conditions were applied and only the nodal values of RI were allowed to vary. Similarly, figures 7(a) and (b) show the internal fluence fields and phase plots, when $n_1 = n_2 = 1.58$, and $n_1 = 1.58, n_2 = 1.33$, respectively.

4. Discussion

In this work, we have presented a method for modelling internal refractive index mismatch for NIR tomography. This approach relies on the application of additional internal boundary conditions within the model to account for the inhomogeneous nature of RI within the region. These additional boundary conditions explicitly imply that the flux across these boundaries is continuous while the fluence rate allows a change due to reflection at the boundary.

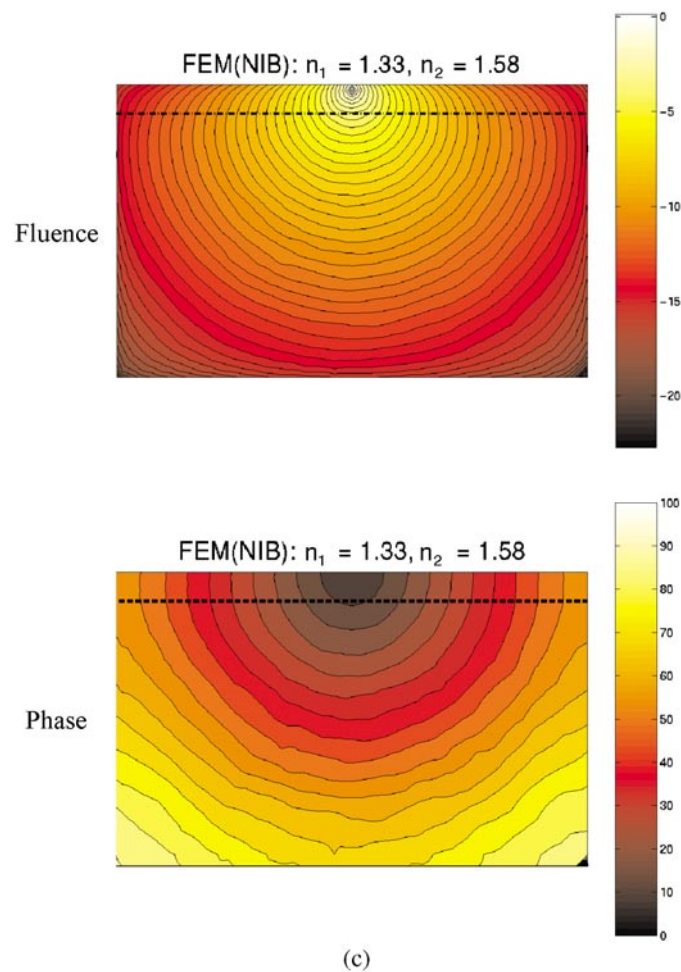


Figure 6. (Continued.)

The method is implemented into a FEM framework and numerical simulations have been performed and compared with Monte Carlo calculations to examine their validity. The model constructed for cross-comparison was a layered slab of homogeneous optical absorption and scattering, but with varying RI in each layer. The RI for each layer was chosen to simulate cases of matched and mismatched media (either 1.33 or 1.56).

In the first case both layers initially had an RI of 1.33 and then the lower layer RI was increased to 1.58. It is important to note the good agreement between the Monte Carlo and FEM data. It can also be seen from the amplitude response that there is little change due an internal RI mismatch, that is to say the intensity of the measured reflectance photons is almost independent of changes in RI. However, looking at the phase, it is evident that there exists a substantial change due to RI variation. As the RI for the bottom layer (n_2) is increased from 1.33 to 1.58 the phase of the measured response is also increased. It is interesting that no change in phase is detected 10 mm away from the source. Furthermore it is evident that assuming just a change in the speed of light in tissue does not predict the measured data accurately. The internal field and phase plots, figures 6(a) and (b), indicate that this change yielded reflections at the lower face of the internal boundary. This caused the light

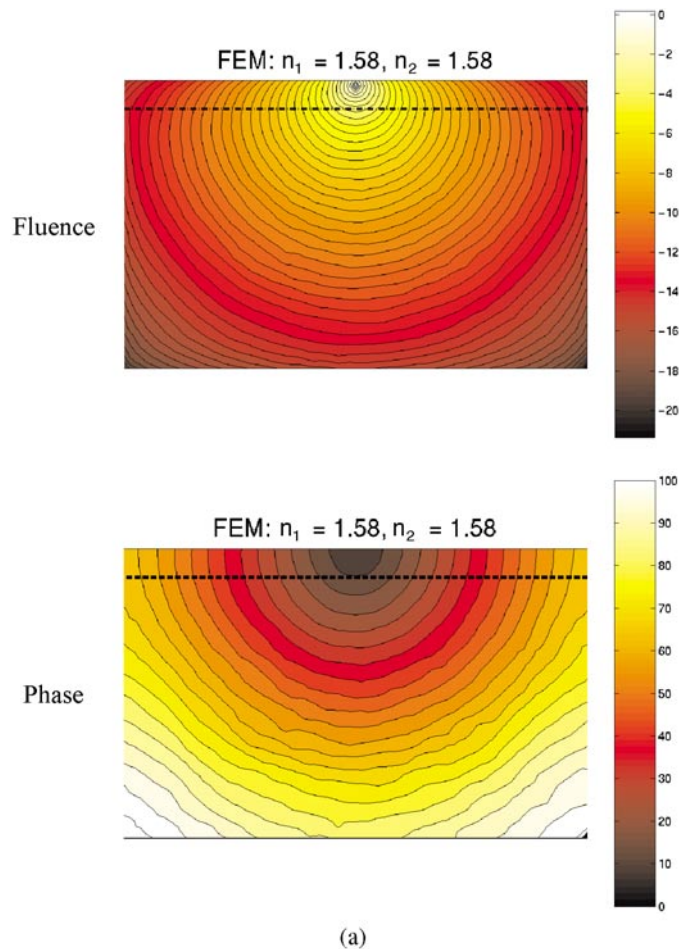


Figure 7. The internal fluence amplitude and phase distribution when (a) $n_1 = n_2 = 1.58$, and (b) $n_1 = 1.58$ and $n_2 = 1.33$. The plot represents the distribution in the cross-section shown by the dashed lines in figure 3.

to take longer to exit at the detector positions (causing an increase in phase compared to the homogeneous case), figure 4(b). However, the total amount of light measured at the detectors was hardly affected by the change in RI, figure 4(a). When the internal boundary conditions were ignored, and only the speed of light was varied, both the internal field and phase plots, figure 6(c), as well as the measured phase data, figure 4(b), at the detector positions were not correct.

From the graphs in figures 6(a) and (b) it is evident that the effect of internal RI mismatch causes the light to be trapped within the bottom layer, due to surface reflection at the internal boundary (represented by the dashed line). This reflection at the bottom face of the boundary forces the light to take longer to exit and emerge at the detector points and therefore resulting in a larger phase change. For comparison purposes, the internal field distribution is also plotted, figure 6(c), where RI is varied for the model, but the internal boundary mismatch is ignored (as shown in the boundary data in figure 4). Here, we can see that although the speed of light at different points may be modelled, the reflection at internal boundaries is completely ignored.

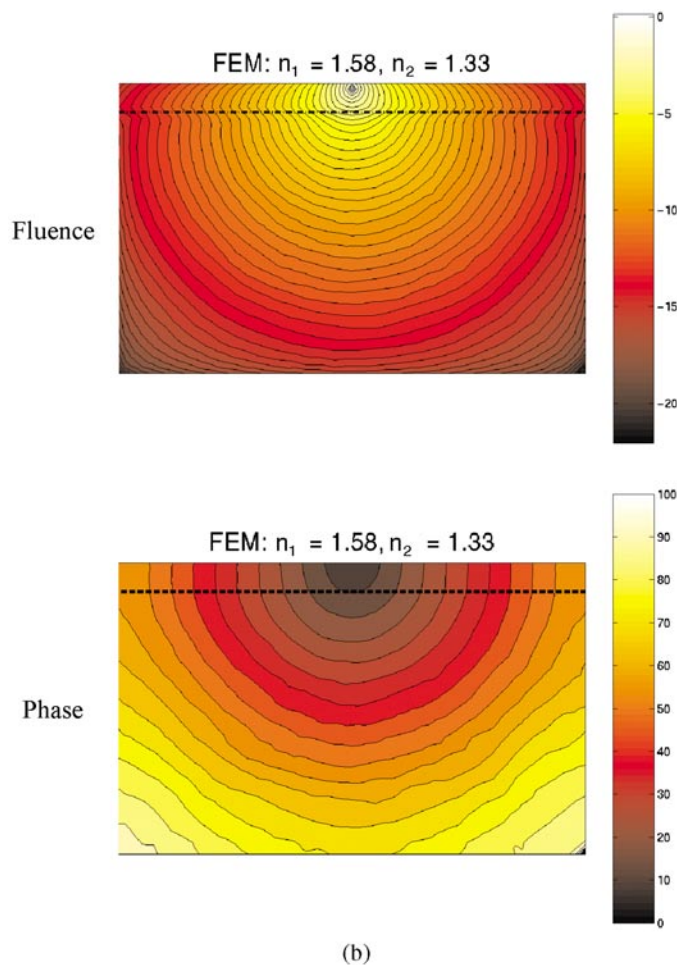


Figure 7. (Continued.)

In the second example where the model represented an RI of 1.58 in the top layer, while the lower layer RI was decreased to 1.33, the light takes less time to exit at the detector positions (causing a decrease in phase compared to the homogeneous case), figure 5(b). However, the total amount of light measured at the detectors is again hardly affected by the change in RI, figure 5(a). From the graphs in figures 7(a) and (b) it is evident that the internal boundary reflection at the top face of layer 2 results in more light being reflected back than is normally expected, causing light trapping in layer 1. This allows light to exit at a faster rate than in a homogeneous case, resulting in the decrease in measured phase as shown in figure 5.

The small change in measured intensity data for the slab model is interesting. The results suggest that the total intensity of light measured is not affected by a change in internal RI. However, as the phase data suggest the time taken for light to travel is significantly altered.

5. Conclusions

A method of implementing internal RI variation within a FEM formulation of the diffusion approximation has been developed. The results for a simple two-layer slab model have been

compared with Monte Carlo calculations. The striking agreement between the data measured with both models suggests that the modified FEM diffusion model is an adequate scheme for describing light propagation within the tissue of varying refractive index. One drawback of this approach is that regions of varying RI need to be known *a priori*. However, the main goal of this paper is to present a method for accurate modelling of this variation, and to provide a tool for numerical analysis of the effect of RI variation.

The results presented here indicate that for a two-layered model, there exists a change in measured phase, but little change in amplitude data. These results may not be completely general, as the model used in this study consisted of a thin layer of 5 mm with a second layer of 45 mm. Also, the RI numbers used were 1.33 and 1.58 and although no absolute values of the RI for biological tissue exist, it may be that tissue RI does not vary significantly within the region of interest (e.g. the female breast). It may be that in a clinical setting, the range of refractive index within the tissue under examination may not be that large; however, further work is needed. Further work is necessary and anticipated to investigate this effect especially in terms of image reconstruction.

Acknowledgments

Funding for this work has been provided by National Cancer Institute through research grants PO1CA80139 and RO1CA69544.

References

- Aronson R 1995 Boundary conditions for diffusion of light *J. Opt. Soc. Am. A* **12** 2532–9
- Arridge S R 1999 Optical tomography in medical imaging *Inverse Problems* **15** R41–R93
- Arridge S R, Dehghani H, Schweiger M and Okada E 2002 The finite element model of the propagation of light in scattering media: a direct method for domains with nonscattering regions *Med. Phys.* **27** 252–64
- Arridge S R, Schweiger M, Hiraoka M and Delpy D T 1993 A finite element approach for modeling photon transport in tissue *Med. Phys.* **20** 299–309
- Bluestone A Y, Abdoulaev G, Schmitz C, Barbour R L and Hielscher A H 2001 Three-dimensional optical-tomography of hemodynamics in the human head *Opt. Exp.* **9** 272–86
- Chance B 2001 Near-infrared (NIR) optical spectroscopy characterizes breast tissue hormonal and age status *Acad. Radiol.* **8** 209–10
- Dehghani H, Pogue B W, Jiang S, Brooksby B and Paulsen K D 2003a Three dimensional optical tomography: resolution in small object imaging *Appl. Opt.* **42** 3117–28
- Dehghani H, Pogue B W, Poplack S P and Paulsen K D 2003b Multiwavelength three-dimensional near-infrared tomography of the breast: initial simulation, phantom, and clinical results *Appl. Opt.* **42** 135–45
- Delpy D T and Cope M 1997 Quantification in tissue near-infrared spectroscopy *Phil. Trans. R. Soc. B* **352** 649–59
- Fantini S, Walker S A, Franceschini M A, Kaschke M, Schlag P M and Moesta K T 1998 Assessment of the size, position, and optical properties of breast tumors *in vivo* by noninvasive optical methods *Appl. Opt.* **37** 1982–89
- Faris G W 2002 Diffusion equation boundary conditions for the interface between turbid media: a comment *J. Opt. Soc. Am. A* **19** 519–20
- Godavarty A, Hawrysz D J, Roy R, Sevick-Muraca E M and Eppstein M J 2002 Influence of the refractive index-mismatch at the boundaries measured in fluorescence-enhanced frequency-domain photon migration imaging *Opt. Exp.* **10** 653–62
- Hebden J C, Veenstra H, Dehghani H, Hillman E M C, Schweiger M, Arridge S R and Delpy D T 2001 Three dimensional time-resolved optical tomography of a conical breast phantom *Appl. Opt.* **40** 3278–87
- Hebden J C *et al* 2003 Assessment of an *in situ* temporal calibration method for time-resolved optical tomography *J. Biomed. Opt.* **8** 87–92
- Hillman E M C, Hebden J C, Schweiger M, Dehghani H, Schmidt F E W, Delpy D T and Arridge S R 2001 Time resolved optical tomography of the human forearm *Phys. Med. Biol.* **46** 1117–30
- Khan T and Jiang H 2003 A new diffusion approximation to the radiative transfer equation for scattering media with spatially varying refractive indices *J. Opt. Soc. Am.* **5** 137–41

- Klose A D and Hielscher A H 1999 Iterative reconstruction scheme for optical tomography based on the equation of radiative transfer *Med. Phys.* **26** 1698–707
- McBride T O, Pogue B W, Jiang S, Osterberg U L, Paulsen K D and Poplack S P 2002 Multi-spectral near-infrared tomography: a case study in compensating for water and lipid content in hemoglobin imaging of the breast *J. Biomed. Opt.* **7** 72–9
- McBride T O *et al* 1999 Spectroscopic diffuse optical tomography for quantitatively assessing hemoglobin concentration and oxygenation in tissue *Appl. Opt.* **38** 5480–90
- Paulsen K D and Jiang H 1995 Spatially varying optical property reconstruction using a finite element diffusion equation approximation *Med. Phys.* **22** 691–701
- Ripoll J and Nieto-Vesperinas M 1999 Index mismatch for diffuse photon density waves at both flat and rough diffuse-diffuse interfaces *J. Opt. Soc. Am. A* **16** 1947–57
- Schmitt J M, Zhou G X, Walker E C and Wall R T 1990 Multilayer model of photon diffusion in skin *J. Opt. Soc. Am.* **7** 2141
- Schoberl J *NETGEN—an automatic 3D tetrahedral mesh generator* <http://www.sfb013.uni-linz.ac.at/~joachim/netgen>
- Schweiger M, Arridge S R, Hiroaka M and Delpy D T 1995 The Finite element model for the propagation of light in scattering media: boundary and source conditions *Med. Phys.* **22** 1779–92
- Takatani S and Graham M 1979 Theoretical analysis of diffuse reflectance from a two-layer tissue model *IEEE Trans. Biomed. Eng.* **26** 656
- Vishwanath K, Pogue B W and Mycek M 2002 Quantitative fluorescence lifetime spectroscopy in turbid media: comparison of theoretical, experimental and computational methods *Phys. Med. Biol.* **47** 3387
- Walker S A, Boas D A and Gratton E 1998 Photon density waves scattered from cylindrical inhomogeneities: theory and experiments *Appl. Opt.* **37** 1935–44
- Wang L, Jacques S L and Zheng L 1995 MCML—Monte Carlo modeling of photon transport in multi-layered tissues *Comput. Methods Programs Biomed.* **47** 131–46
- Xu H *et al* 2003 Near-infrared imaging in the small animal brain: optimization of fiber positions *J. Biomed. Opt.* **8** 102–10